

Applications of scanning electron microscopy in earth sciences

CHEN Li*, XU Jun & CHEN Jing

Electron Microscopy Laboratory, School of Physics, Peking University, Beijing 100871, China

Received December 24, 2014; accepted July 20, 2015; published online August 19, 2015

This paper expounds upon the basic principle of scanning electron microscopy (SEM), the main features of image types, and different signals, and the applications and prospects in earth sciences research are reviewed. High-resolution field emission SEM allows observation and investigation of a very fine micro area *in situ*. Using low-vacuum mode SEM, geological insulating samples can be analyzed directly without coating, demonstrating the wide application prospect. Combined with backscatter detector (BSE), energy dispersal X-ray spectroscopy (EDS), cathodoluminescence spectrometry (CL), and electron back-scattering diffraction (EBSD), SEM can yield multiple types of information about geological samples at the same time, such as superficial microstructure, CL analysis, BSE image, component analysis, and crystal structure features. In this paper, we use examples to discuss the geological application of SEM. We stress that we should not only focus on the CL image analysis, but strengthen CL spectrum analyses of minerals. These results will effectively reveal the mineral crystal lattice defects and trace element composition and can help to reconstruct mineral growth conditions precisely.

scanning electron microscopy, signal detector, minerals

Citation: Chen L, Xu J, Chen J. 2015. Applications of scanning electron microscopy in earth sciences. *Science China: Earth Sciences*, 58: 1768–1778, doi: 10.1007/s11430-015-5172-9

SEM provides direct, real-time, high-resolution data with stereo viewing capabilities; offers a great depth of focus; and requires easy sample preparation. SEM is one of most important members among the micro-beam analysis instruments. SEM is an essential observation tool to investigate micro-characteristics of samples in natural science; it has also been widely used in the field of geological scientific research.

New SEM can load multiple attachments, including BSE, EDS, EBSD and CL, which considerably enhance the ability of the analysis. Except for the morphology of samples, we can obtain information regarding composition micro-analysis, crystal structure features, BSE images, CL images and spectra. For example, a zircon CL image can be used to reveal the geneses of zircons with complicated interior

structures and to recuperate the zircon crystallizing processes. Thus, reliable bases can be provided for the choices of the analyzing sites of micro area dating and reasonable interpretation of the acquired U-Pb ages. The development of zircon U-Pb geochronological studies has been greatly promoted (Ames et al., 1993; Wilde et al., 2001; Lissenberg et al., 2009; Zhang et al., 2009, 2014, 2015). An EBSD fabric diagram of minerals can be obtained rapidly and accurately and is critical for determining the rheological mechanism and dynamics of the rock. Then, information about the rock formation conditions and the deformation mechanism would provide constraints for convergent plate boundary study (Jin et al., 2001; Brenker et al., 2002; Xu et al., 2005).

For geological samples, there are two advantages of using SEM. The first advantage is the simple sample preparation process; for example, there is no need to coat non-conductive samples. Second, along with the high-resolution imaging of the sample, we can generate more information

*Corresponding author (email: chenli@pku.edu.cn)

using EDS, EBSD, CL or BSE.

In general, SEM performance has been constantly improved and enhanced, which greatly promotes the quantitative research of geological science. SEM has become one of the most versatile instruments available for the examination and analysis of the microstructural characteristics of solid objects. In this paper, we expound upon the basic principle of SEM and the properties of the various signal detectors. Then, combined with some examples of the research in recent years, the application of SEM in earth sciences is discussed.

1 The basic principle of SEM

The basic principles of SEM were established by Knoll and von Ardenne (Germany) as well as Zworykin and Hillier (USA), during the 1930s and early 1940s. In 1942, the first SEM instrument was applied to examine thick specimens with a 1 μm resolution and was built by Zworykin RCA laboratory in the United States. In 1960, Everhart and Thornley improved the secondary electron detector. Now, the E-T secondary electron detector is the mainstream detector of SEM. Then, SEM entered the commercialization stage. In 1967, the electron channeling contrast that was produced by the interaction of electrons and the lattice pattern was observed. This contrast was developed as the widely used technology of EBSD. In the 1980s, the EDS/WDS analysis began to join with SEM. Because of various mature commercial detectors around SEM, the application of SEM has greatly expanded. In 1990, SEM entered the era of digital

imaging.

In recent years, with the rapid development of science and technology, the brightness of the field emission gun is approximately 1000 times greater than that of tungsten emission. Using the field emission gun, a monochromator, low-aberration objective lens and high-sensitivity signal detector in the instrument, a resolution of 1 nm is achieved with field-emission SEM. Even under a low voltage (e.g., 1 kV), SEM imaging still performs well. Thus, we can obtain mineral information at the nanoscale level. Variable-pressure scanning electron microscopy (VPSEM) permits the examination of almost any specimen because the environment around the specimen no longer has to be at high vacuum (Danilatos, 1982a, 1982b). Thus, the surface information would be real and complete.

Today, the commonly used SEM instruments are the following models: S-5200 and S-4800 SEM made by Hitachi company and the Quanta series and Nova Nano series SEM made by FEI company.

1.1 The basic structure and working principle of the SEM

The SEM instrument is made up of four basic parts (Figure 1): (1) the electron optical systems, include electron gun, electron lens, scan coils, astigmatism and aperture; (2) the chamber; (3) the signal detector, processing and display system; and (4) the vacuum system.

The basic working principle of SEM: the electron gun generates electrons and accelerates them to an energy range of 0.1–30 keV. The spot size from a tungsten hairpin gun is

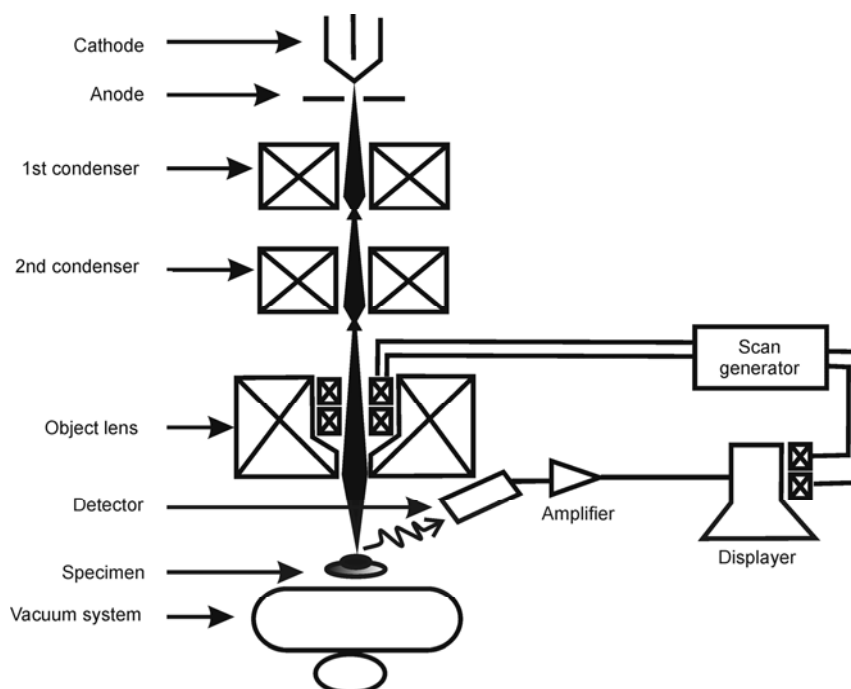


Figure 1 Schematic drawing of the electron column showing the electron gun, the lenses, the deflection system, and the electron detector.

demagnified to a sharp image by means of electron lenses, as shown schematically in Figure 1. Most SEM instruments can produce an electron beam at the specimen with a spot size of less than 10 nm that contains sufficient probe current to form an acceptable image. The beam emerges from the final lens into the specimen chamber, where it interacts with the specimen to a depth of approximately 1 μm and generates the signals that are used to form an image, such as BSE, SE and CL. These signals can be collected and amplified by different detectors. The electronics of the detector system convert the signals to point-by-point intensity changes on the viewing screen and produce an image. The contrast of images depends on the property and yield of the signals that are collected by the detector.

1.2 Types and features of the signal in SEM

There are two main types of electron beam-specimen interactions: elastic scattering and inelastic scattering. Elastic scattering can result in beam electrons leaving the specimen (a process called “backscattering”), providing an important class of information for SEM imaging (BSE and EBSD). Inelastic scattering gives rise to useful signals, such as secondary electrons, auger electrons, characteristic X-rays and CL. These signals are obtained from specific emission volumes within the sample and can be used to examine many characteristics of the sample (surface topography, crystal-

lography, composition, spectrum, etc.).

1.3 Brief introduction of the SEM application in earth sciences

Geological samples are mainly rocks or fossils, in which minerals are mainly composed of silicate, oxide, sulfide, etc. Using SEM, we can determine the surface topography of samples. Meanwhile, other characteristics of the sample can be examined, such as BSE images, crystallography, composition, and spectra (Figure 2).

2 The characteristics of BSE and its application in earth sciences

2.1 The characteristics of BSE

Backscattered electrons are produced by incident electron scattering by the nucleus of the sample. The yield increases strongly with the atomic number of the sample. Therefore, the contrast in the BSE image can reflect the distribution of heavy or light elements, whose area is observed. Especially for geological samples, different mineral phases will be easy to differentiate, coupled with EDS in the BSE image.

2.2 Application of BSE in earth sciences

The yield of the BSE is proportional to the average atomic

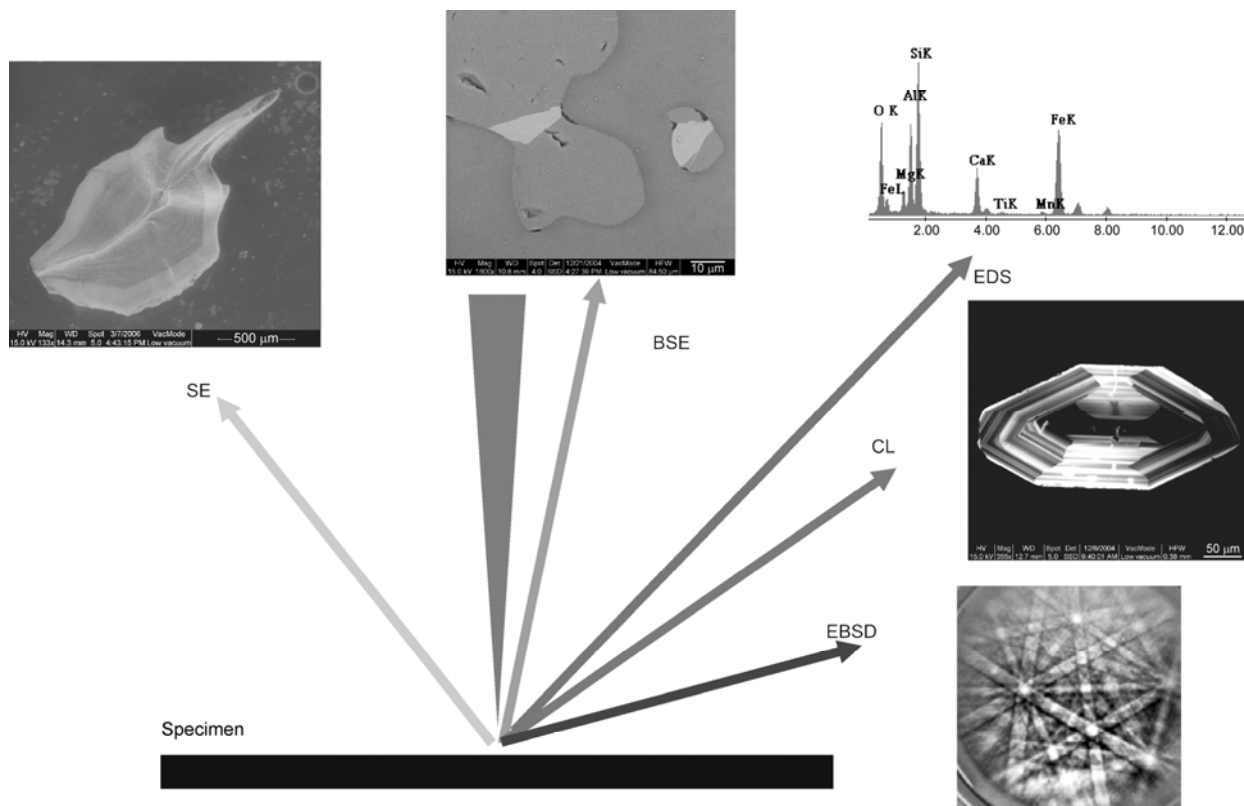


Figure 2 The types of signals that are produced from the interaction of the electron beam with the samples.

numbers of the sample. Thus, atomic number contrast can clearly distinguish different mineral phases and different compositions of one mineral grain in the BSE image. Because most geological samples are mineral aggregates, the SE image (surface topography) generally cannot distinguish different minerals. Therefore, it is more useful to generate a BSE image for geological samples (Smieja-Król and Fiałkiewicz-Kozieł, 2014; Li and Xiao, 2012). To generate a good BSE image, the sample must be smooth. Otherwise, the coarse surface of the sample will affect the contrast of the image. A thin section or polished rock samples can be used for BSE.

Some types of exsolution textures would often be found in the main rock-forming minerals of the UHP metamorphic rocks (garnet, pyroxene, olivine, etc.). These textures usually affect indicators of the rock formation conditions and the deformation mechanism, such as temperature, pressure and geochemical conditions of the geological background (Ye et al., 2000; Zhu and Ogasawara, 2002; Yang et al., 2005). For example, inclusions are observed in the exsolution texture of the magnetite and titanomagnetite along the {111} lattice ilmenite surface in the gabbro (Dziony et al., 2014), the exsolution texture of titanclinochumite and titanochondite in the clinopyroxene (Xu et al., 2003), and the exsolution texture of pargasite and ilmenite in clinopyroxene (Chen and Xu, 2005) (Figure 3). Because the atomic number contrast dominates the image, the exsolution lamella can be easily distinguished from the host mineral under the BSE image. In Figure 3, the average atomic number of pargasite (prg) is the lowest in the rock, while that of ilmenite (ilm) is the highest. Therefore, ilmenites are shown as the brightest minerals in the image.

3 The characteristics of the secondary electron and its application in earth sciences

3.1 The characteristics of the secondary electron

Secondary electrons, which are generated by inelastic scattering of incident electrons, are electrons with less than 50 eV of energy that are emitted from the samples. Only surface electrons within a depth range of 5–50 nm could escape the samples to become secondary electrons. Thus, the yield of secondary electrons is relevant to the surface topography of the sample, and the secondary electron image can reflect the shape of the sample. In particular, with the application of field emission scanning electron microscopy and using a high-resolution secondary electron (SE_i) imaging technique, topography with a resolution as small as 1 nm can be achieved, yielding topography information at the nanoscale level.

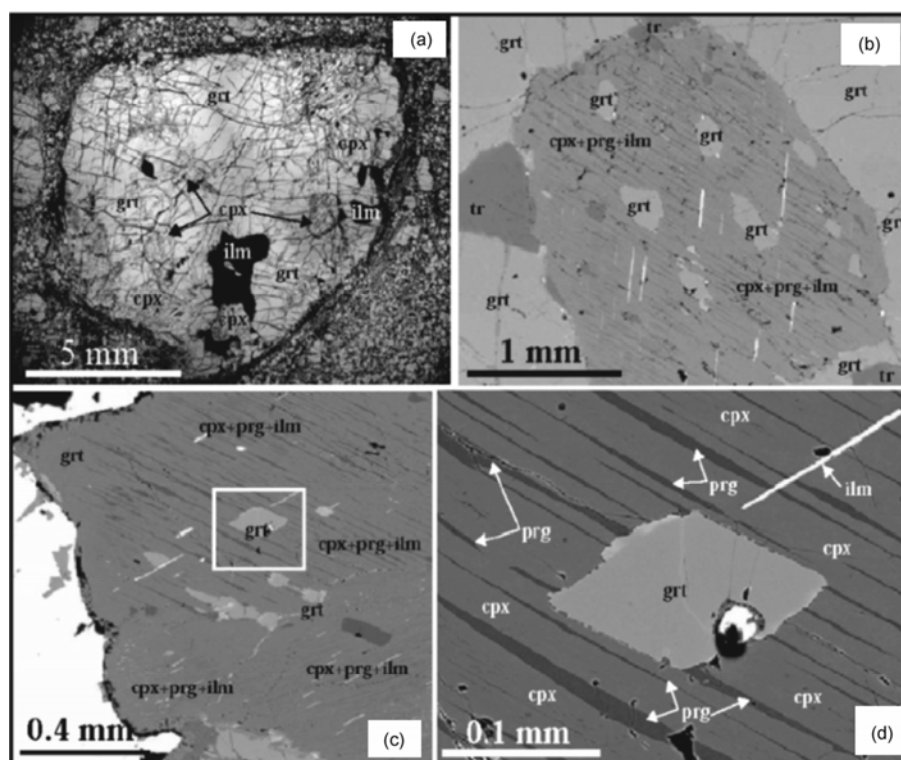


Figure 3 Clinopyroxene with pargasite and ilmenite exsolution textures occurring as inclusion in garnet of garnet-pyroxenite sample (Chen and Xu, 2005). (a) Garnet porphyroblast contains clinopyroxene inclusions in garnet-pyroxenite, plane-polarized light; (b) BSE images show clinopyroxene (cpx) with pargasite (prg) and ilmenite (ilm) exsolution textures occurring as inclusion in garnet (grt); (c) BSE image shows diopside with pargasite and ilmenite exsolution textures and garnet inclusions; (d) enlarged BSE image shows the relations among pargasite and ilmenite exsolution lamellae and garnet inclusions in clinopyroxene.

3.2 Application of secondary electron imaging in earth sciences

The secondary electron image is a morphological image that is produced by SEM. We can observe the morphology from the micron to the nanometer scale. In terms of sample preparation, massive, powder or thin-section samples can be directly observed. For example, in the sectional view of the tubular structures of natural serpentine (Figure 4), the outer diameter of the tube is approximately 30–50 nm, and the inner diameter is approximately 6–9 nm. Because the sample is brittle, it is difficult to prepare as a TEM sample; however, it is relatively easier to cut a larger cross-sectional sample after embedding for SEM.

Along the direction of the arrow, the internal diameter of the tube is approximately 8 nm, and the outside diameter is approximately 35 nm.

The morphology of minerals determined by SEM can be used to analyze and speculate about the mineral formation process and the related geological environment. For example, in different environments, the quartz surface morphology will be different. The particles that are formed by wind generally have a pockmarked face and butterfly pit on the surface, and a strong wind will cause a crescent-shaped impact crater on the surface. Quartz particles that are formed by water generally have V-shaped energy pits; the size, the number, the depth and the distribution pattern of this V-shaped pit will be related to the water flow energy. In contrast, quartz particles that are formed by glaciers often have sharp edges and a conchoidal fracture (Wu et al., 1996; Xie and Cui, 1981). In fault gouges, the pores and grain boundaries between quartzes reflect the sliding direction and the sliding type of the fault (Mancktelow et al., 1998).

In addition, SEM is often used in paleontology (Dong et al., 2004; Bengtson and Zhao, 1997; Balinski and Sun, 2008). Some samples of precious fossil embryos have irregular

shapes. When using conventional SEM, it is necessary to coat a very thick conductive film before observation, concealing many details. However, using low-vacuum SEM, we can directly observe the sample without coating. Sample stage rotation or tilt can result in images on different sides, which will help restore the fossil embryos of three-dimensional graphics (Donoghue et al., 2006; Chen et al., 2008).

4 The feature element-characteristic X-rays and their application in earth science

4.1 The feature element-characteristic X-rays

Element-characteristic X-rays are generated by inelastic incident electron scattering through the sample. While electrons in the sample atoms' inner-shell are excited, outer electrons transit and produce X-rays with characteristic information about the elements. Through X-ray energy dispersal spectroscopy (EDS), micro-area ingredients and compositional information can be examined. EDS can provide qualitative results of components and semi-quantitative or quantitative compositions of samples and the distribution of elements in the sample through line scan and mapping.

4.2 Application of EDS in earth sciences

Generally equipped with EDS, SEM can perform composition analysis during morphological observation. Currently, EDS analysis covers a range of ${}_{5}\text{B}$ – ${}_{92}\text{U}$. When performing the spectrum analysis, the accelerating voltage of SEM should be 2–3 times the X-ray energy of the measured elements. Thus, when the characteristic X-ray energy of the sample is high, the accelerating voltage should also be high. Otherwise, the acceleration voltage should be low; thus, we can reduce the electron beam's effect depth in the sample and improve the spatial resolution of the compositional analysis. Generally, the samples that meet the topography analysis requirement can also be used for spectrum analysis. The sample surface should be smooth and neat while performing line scan or mapping.

Compared to wavelength spectrometry (WDS) in an electron microprobe, the X-ray spectrum analysis of SEM has several advantages: (1) high analysis speed, it generally only needs several seconds to several minutes to complete a full-spectrum analysis; (2) small beam spot, it can perform a micro-area analysis of samples ranging from several micrometers to hundreds of nanometers with a high spatial resolution of the component analysis; (3) it can perform an integrated analysis of the sample's composition, morphology and structure.

Geological samples are generally a variety of mineral aggregates. SEM combined with EDS can provide component identification and semi-quantitative analysis for fine minerals. For example, some clay minerals in sedimentary rocks (<2 μm), such as illite, smectite and chlorite, are

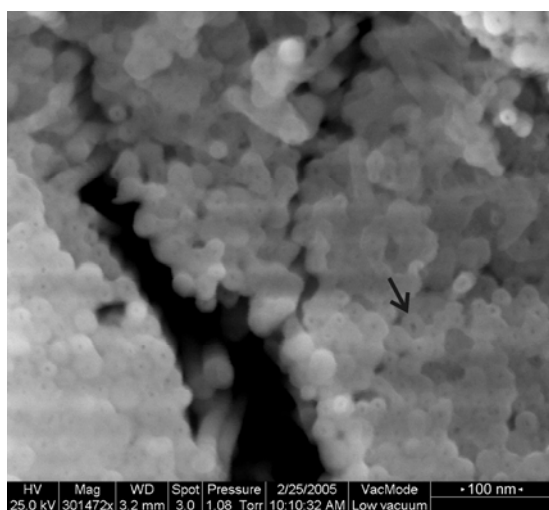


Figure 4 Natural serpentine tubular structures. Secondary electron image, 300000 \times (Wang, 2005).

difficult to distinguish from each other in shape and morphology, while EDS can distinguish these minerals quickly and effectively (Li and Xiao, 2012; Smieja-Krół and Fiałkiewicz-Kozieł, 2014; Rajkumar et al., 2014). Using line scanning, it is possible to analyze the variation in the mineral composition in one direction (Gao et al., 2013). Using component mapping, we can analyze the element distribution in an area of a sample. For example, using SEM, we can clearly observe the enstatite (MgSiO_3) reaction rim of the forsterite (Mg_2SiO_4) and quartz (SiO_2); the reaction formula is $\text{Mg}_2\text{SiO}_4 + \text{SiO}_2 = 2\text{MgSiO}_3$. Through mapping analysis, we can clearly identify the diffusion directions of the Mg (outward) and Si (inward) (Abart et al., 2004). In Figure 5, we can identify the distribution of Si and Mg in the area distribution of minerals using EDS; however, we cannot identify the mineral phase. In Figure 5(a), using the BSE detector, we can identify three mineral phases—quartz, enstatite and forsterite. Therefore, combined BSE and EDS is often used in mineral samples.

Most of the geological samples are non-conductive. Therefore, additional element information from outside of the detection area is often generated in low-vacuum mode because of electron beam scattering. Electron beam scattering will occur when high-energy electron beams encounter gas-water vapor or other gases, which are in the sample chamber in low-vacuum mode. The electron beam scattering radius is closely related to the sample chamber's pressure, acceleration voltage and working distance (Danilatos, 1988). The working distance is theoretically constant when the accelerating voltage increases, and when the pressure decreases, the scattering radius becomes smaller.

There are two ways to solve the energy spectrum error

that is caused by electron beam scattering. One method is to apply a vapor deposit conductive coating to the samples and to perform the spectrum analysis in high-vacuum mode. The other method is to perform the spectrum analysis in low-vacuum mode using the spectrometer software for correction. The specific spectrometer correction software works as follows: select an area and take a spectrum at high pressure (130 Pa), and then repeat the process at low pressure (10 Pa) and make a comparison of the two results to calculate the difference that is caused by electron beam scattering. Using resin-embedded Cu_2S sample spectrum analysis, Berre et al. (2007) compared the energy spectrum correction methods under two low-vacuum conditions. The conclusion was that the software correction method is very effective. In addition, when performing the line scanning and mapping of non-conductive samples, the samples should be analyzed in high-vacuum mode after coating. Because the software correction method does not apply to line scanning and mapping, electron beam scattering caused in low-vacuum mode can affect the accuracy of the scan.

5 The characteristics of CL and its application in earth sciences

5.1 The characteristics of CL

CL is generated when incident electrons enter samples and cause inelastic scattering. When some solid-material samples (such as semiconductors, minerals and some organic molecular materials) are subjected to electron irradiation, their valence electrons are excited to a higher energy level or energy band, and the excited material produces relaxation

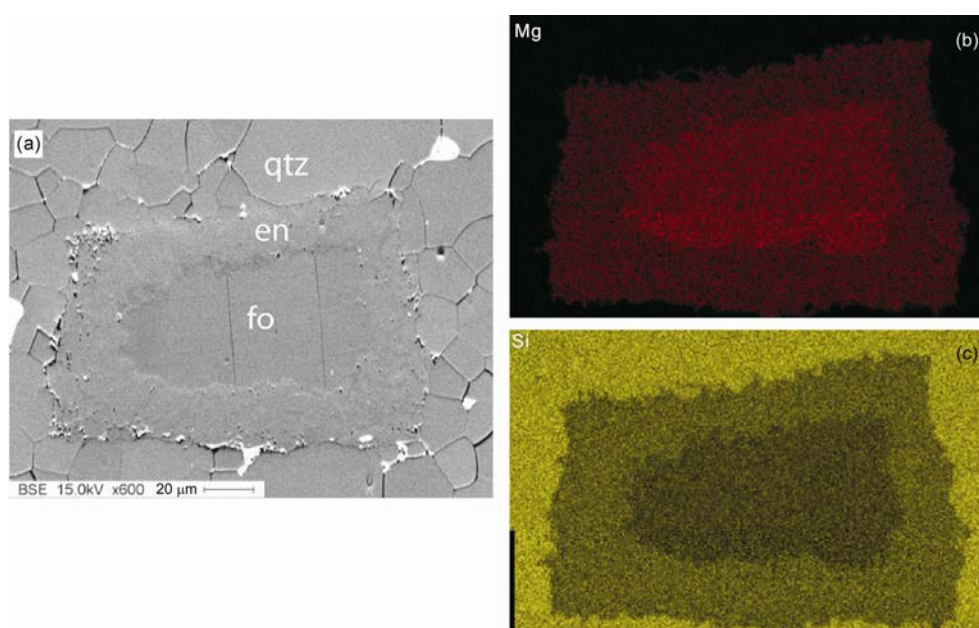


Figure 5 Distribution of elements in the enstatite reaction rim of the forsterite and quartz (Abart et al., 2004). (a) BSE image; (b) distribution of Mg; (c) distribution of Si; qtz, quartz; en, enstatite; fo, forsterite.

light. There are three types of situations that cause electronic excitation to generate CL. The first situation is band-band luminescence, which means that when excited by additional electrons, the electrons transit from the conduction band to the valence band. The excited electrons will generate luminescence when returning to the conduction band. This band-band luminescence can showcase the characteristic properties of minerals. The second situation is called defect luminescence, which means that the excited electrons do not return to the conduction band but arrive at the defect position and emit luminescence. The third situation is called impurity luminescence, which means that when inter-band impurity was excited by additional electrons, luminescence will be generated (Nasdala et al., 2003).

5.2 Application of CL in earth sciences

CL spectrometry can be operated in panchromatic or monochromatic mode. The wavelength is in the range of 200–2100 nm. We can obtain panchromatic/monochromatic imaging and spectra using the CL spectrometer. Moreover, CL can be performed at the micron or nanometer scales. CL can clearly reflect the internal structure of the mineral. The CL spectrum can reflect lattice defects and the presence of impurities. CL requires the sample surface to be smooth and flat, and a single mineral particle can be polished after being embedded.

Among geological samples, many types of minerals can generate cathodoluminescence after being excited by electrons, such as zircon, feldspar (Kayama et al., 2010; Richter et al., 2002), quartz (Götze and Richter, 2006), apatite (Mitchell et al., 1997) and carbonate (Habermann et al., 1996). At present, the most commonly observed mineral is zircon.

Zircon is widely present in a variety of genetic rocks. Its CL image may well reveal the internal phases and causes that are characterized by different zonal structures. In the process of U-Pb geochronological microanalyses using SHRIMP or LA-ICPMS, the precise localization of analyzed spots and a reasonable interpretation of the results depend more on the high-quality CL images. Using environmental SEM or low-vacuum scanning electron microscopy, we can choose the low-vacuum mode in order to avoid contamination and damage to the samples. Because the CL images of magmatic zircons and metamorphic zircon are quite different, CL has become an important research tool to identify genetic types of zircon. Magmatic zircons are formed in a freely growing suspended lava environment, usually leading to euhedral/semi-euhedral crystal shapes of cylinder and double cone; in contrast, metamorphic zircons typically having a rounded, allotriomorphic shape or subhedral shape and various interior structures, including non-zonation, and weak, misty, fan-shaped, fir needles-like, facial, spongy, and streaming zonations (Figure 6) (Corfu et al., 2003; Vavra et al., 1996, 1999)

Zircons with different geneses also have significantly different CL spectra (Hanchar and Rudnick, 1995; Chen et al., 2006; Zhang et al., 2008). Magmatic zircon's spectrum is generally strong and sharp, while metamorphic zircon has a weak and blunt peak (Figure 7). Zircons formed under different pressures (20–60 GPa) also showed significant differences in their CL spectra (Gucsik et al., 2002). The peak positions of zircon fall mainly at wavelengths of 313, 481 and 579 nm. A study by Nasdala (2003) on zircon CL spectra in the visible region suggests that luminescence at wavelengths of 481, 579 and 754 nm is triggered by the rare earth element Dy^{3+} in the zircon; luminescence at wavelengths of 579, 626 and 663 nm is triggered by the element Sm^{3+} .

Furthermore, the luminescence of mineral impurities can reflect the physical chemistry environment when the lattice is formed. For example, the luminescence at the edges of apatite is mainly caused by Mn^{2+} impurities, while the luminescence in the center is mainly caused by rare earth elements (Figure 8) (Götze, 2012).

6 The characteristics of EBSD and its application in earth sciences

6.1 The characteristics of EBSD

When electron beams graze through the sample at a large angle, the incident electrons are scattered by the sample lattice, resulting in the lattice channel effect caused by backscattered electrons, which can be obtained by EBSD imaging. Through EBSD pattern analysis, we can obtain the detailed crystallographic characteristics of the mineral at the micron or nanometer scale.

6.2 Application of EBSD in earth sciences

EBSD technology makes possible the *in situ* and microscale research of rock and mineral, allowing determination of the mineral phase and yielding crystal structure information. Based on backscatter diffraction pattern spectrum analysis, we can quickly identify the crystal face symbol, mineral crystal, crystal belt and cell parameters (Prior et al., 1999; Humphreys, 2004). EBSD analysis has strict requirements for sample preparation; for example, the sample surface must be finely polished. The polishing time, strength and tools should be decided in accordance with the intensity of the sample. Application of EBSD in geology study includes the following.

(1) Mineral phase appraisal. For unknown mineral phases, we should obtain the EBSD image and the back scattering diffraction patterns of the unknown mineral and then perform a structure analysis using the XRD database, combined with an EDS analysis of information to determine the composition of the mineral phase. For mineral phases with known composition, such as isomorphism and heterophany,

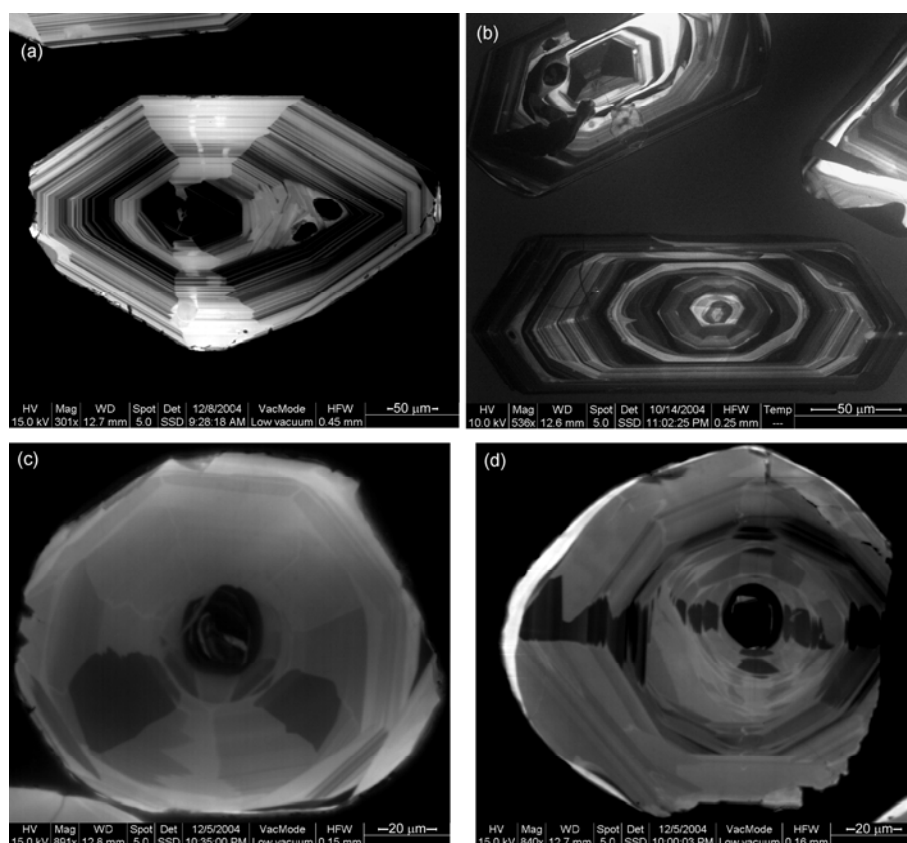


Figure 6 Zircon CL images. (a) A magmatic zircon from gabbroic complex rocks (Xiao et al., 2003); (b) magmatic zircons from gabbroic complex (Sun et al., 2004); (c), (d) a metamorphic zircon from the granulites in Yushugou terrain (Zhou et al., 2004).

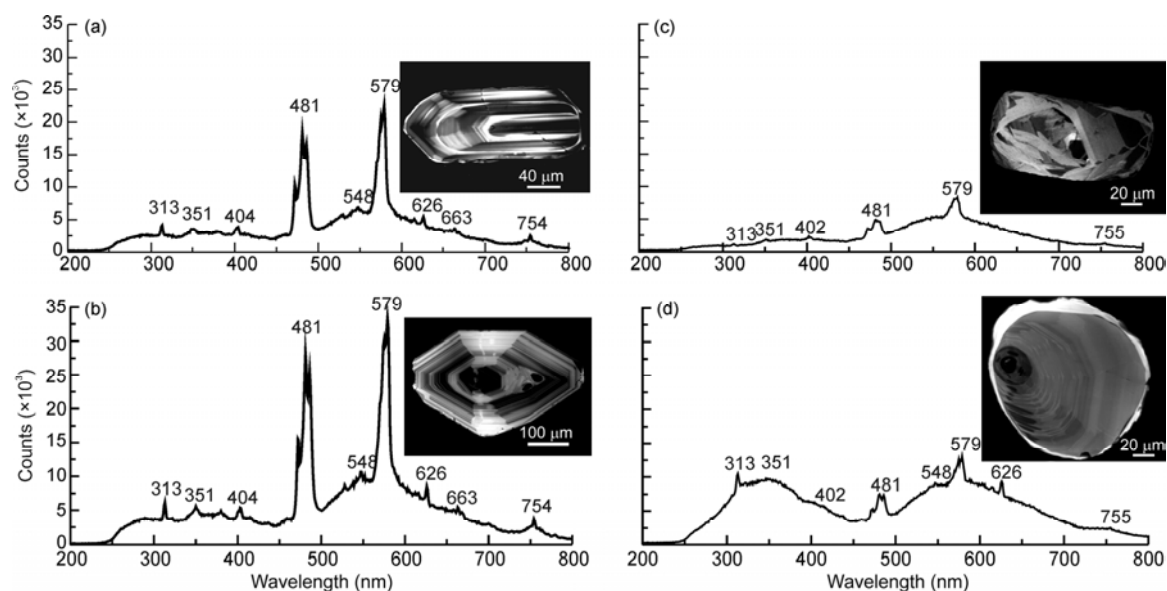


Figure 7 Different genetic types of zircon CL spectra (Chen et al., 2006). (a), (b) magma crystallization zircon; (c), (d) metamorphic zircon.

we can identify the mineral phases directly through the backscatter diffraction patterns and the characteristics of the crystal structure (Stöckhert et al., 2001).

(2) Calculate and measure the lattice orientation of the specific minerals. EBSD can automatically and quickly ob-

tain mineral orientation data, which is the best instrument to calculate the preferred mineral orientation to draw a fabric diagram or polar diagram. In microscopy studies, EBSD can help solve the difficulties of using an optical microscope and a Fedorov stage to obtain crystallographic directions

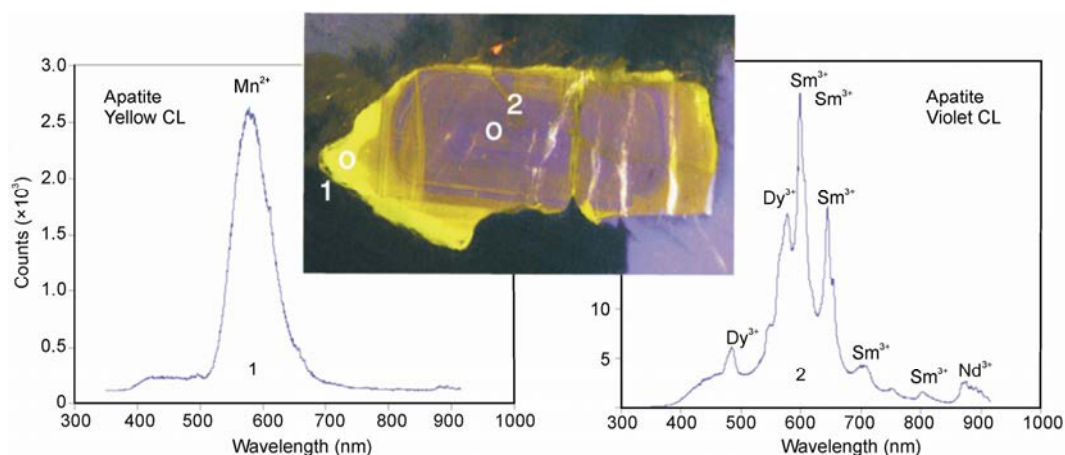


Figure 8 CL image of apatite in granite and the spectra of two positions. 1, edge of apatite shows yellow emission by impurities Mn^{2+} ; 2, center of apatite shows purple emission by REEs.

manually, which is rather complicated and inaccurate. In contrast, EBSD is a great tool to access large amounts of data and to plot a fabric diagram simply and quickly, highlighting statistical significance. EBSD could provide important implications for the interpretation of tectonics, the calculation of temperature and pressure conditions of metamorphism and deformation; the seismic velocity broadcast mechanism, and the transport mechanisms of minerals (Xu et al., 2009; Zhang et al., 2005). For example, increases in the water content of olivine at high temperatures can promote olivine dislocation slipping along the [001] direction, changing the olivine crystal priority directions and leading to the division of five olivine fabric catalogs (Jung and Karato, 2001, Katayama et al., 2004).

Type A: (010) [100] oriented slip system, formed under low-stress and low-water-content conditions.

Type B: (010) [001] oriented slip system, formed under high-water-content and high-stress conditions.

Type C: (100) [001] oriented slip system, formed under moderate-stress and high-water-content conditions.

Type D: {0kl} plane nearly parallel to the shear plane and [100] axis nearly parallel to the shear direction, formed under high-stress and low-water-content conditions.

Type E: (010) [100] oriented slip system, formed under moderate-water-content and low-stress conditions (Figure 9).

(3) Accurately and visually measure the orientation of mineral phases. EBSD can be used to accurately measure the orientation between mineral phases or the interfacial angle of the same type of mineral and can be used to determine the small-angle grain boundaries and twin planes (Abart et al., 2004).

7 Conclusions

Recent geological sampling analyses show that field emission

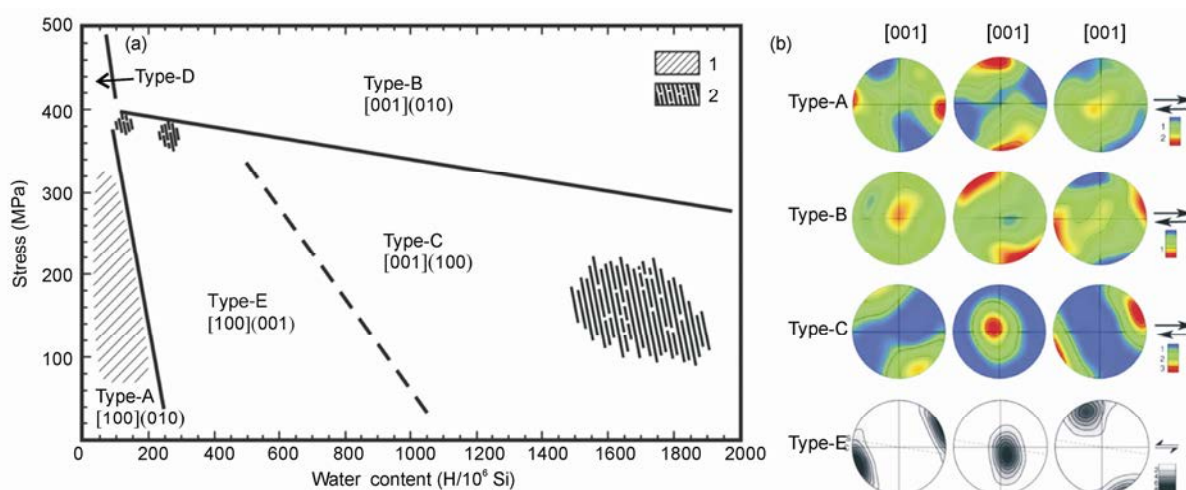


Figure 9 Association between olivine fabrics and stress-water content at a temperature of 1470–1570 K (Katayama et al., 2004) (a) and olivine crystal-axis-preferred orientation polar map (b). (a) 1, olivine sample projection (Zhang et al., 2000); 2, olivine projection in sesame garnet peridotite (Xu et al., 2005). (b) Type-A–D from Jun et al. (2001), type-E from Katayama et al. (2004), with X axis as the direction of the stretching lineation, XY plane as the foliation, and Z axis as the vertical direction.

SEM assembled with other equipment, including BSE, EDS, CL and EBSD, has a wide range of applications in earth sciences. With a sharp increase in the resolution of SEM (better than 1 nm) in recent years, especially after the emergence of high-resolution low-vacuum SEM, nonconductive rock or mineral samples can be directly analyzed, including surface fine image, compositional analysis and even crystal structure analysis, without complication and can easily lead to sample contaminated coating, making experimental analysis more convenient and characteristic information more realistic and helping with the follow-up experimental work of the samples.

In addition, loaded with multi-probes, the testing capability of the new field emission SEM has greatly expanded. Equipped with the BSE probe and X-ray spectrometer probes, SEM can quickly and accurately measure the micro components of the samples. At the same time, we can obtain element distributions of the samples through line scanning and maps, helping showcase the element changes and migration patterns of the mineral phases and explore the growth conditions and deuteric alteration of the minerals. Combined with EBSD, SEM is able to identify the mineral phase changes and obtain *in situ* and micro-scale information of crystal structure and grain orientation.

SEM in conjunction with CL spectrometry captures high-definition CL images of the internal structure of zircon, providing an important basis for the rational selection of the *in situ* U-Pb dating sites of zircon and the accurate interpretation of the analysis results. In addition, there are many minerals in geological samples (such as feldspar, quartz, apatite, etc.) that will emit luminescence after being excited by an electron beam. Therefore, mineralogical comparison studies using a CL spectrum have demonstrated the unique application prospect in revealing mineral lattice defects, trace element distributions and other aspects.

We thank Dr. Su Li for offering zircon samples and constructive suggestions, anonymous reviewers and Dr. Li Xianhua for their constructive suggestions. This work was supported by the National Natural Science Foundation of China (Grant No. 41402031).

- Abart R, Kunze K, Milke R, Sperber R, Heirich W. 2004. Silicon and oxygen self-diffusion in enstatite polycrystals: The Milke et al. (2001) rim growth experiments revisited. *Contrib Mineral Petrol*, 147: 633–646
- Ames L, Tilton G R, Zhou G. 1993. Timing of collision of the Sino-Korean and Yangtze cratons: U-Pb Zircon dating of coesite-bearing eclogites. *Geology*, 21: 339–324
- Balinski A, Sun Y. 2008. Micromorphic brachiopods from the Lower Carboniferous of South China, and their life habits. *Foss Str*, 54: 105–115
- Bengtson S, Zhao Y. 1997. Fossilized metazoan embryos from the earliest Cambrian. *Science*, 277: 1645–1648
- Berre J, Demopoulos P, Gauvin R. 2007. Skirting: A limitation for the performance of X-ray microanalysis in the variable pressure or environmental scanning electron microscope. *Scanning*, 29: 114–122
- Brenker F E, Prior D J, Muller W F. 2002. Cation ordering in omphacite and effect on deformation mechanism and lattice preferred orientation (LPO). *J Struct Geol*, 24: 1991–2005
- Chen F, Dong X P. 2008. The internal structure of Early Cambrian fossil embryo *Olivoooides* revealed in the light of Synchrotron X-ray Tomographic Microscopy. *Chin Sci Bull*, 53: 3860–3865
- Chen J, Xu Z Q. 2005. Pargasite and ilmenite exsolution texture in clinopyroxenes from the Hujialing garnet-pyroxenite, Su-Lu UHP terrane, Central China: A geodynamic implication. *Eur J Mineral*, 17: 895–903
- Chen L, Xu J, Su L. 2006. Application of cathodoluminescence to zircon in FEG-ESEM. *Prog Nat Sci*, 16: 919–924
- Corfu F, Hanchar M, Hoskin P, Kinny P. 2003. Atlas of zircon textures. *Rev Mine Geochem*, 53: 469–500
- Danilatos G D, Postle R. 1982a. The environmental scanning electron microscope and its applications. *Scan Electron Microsc*, 1–16
- Danilatos G D, Postle R. 1982b. Advances in environmental and atmospheric scanning electron microscopy. *Micron*, 13: 253–254
- Danilatos G D. 1988. Foundations of environmental scanning electron microscopy. *Adv Electron Electr Phys*, 71: 109–250
- Dong X P, Donoghue P C J, Cheng H, Liu J B. 2004. Fossil embryos from the Middle and Late Cambrian period of Hunan, south China. *Nature*, 427: 237–240
- Donoghue P, Bengtson S, Dong X P, Gostling N, Hultgren T, Cunningham J, Yin C Y, Yue Z, Peng F, Stamparoni M. 2006. Synchrotron X-ray tomographic microscopy of fossil embryos. *Nature*, 442: 680–683
- Dziony W, Horna I, Lattard D. 2014. *In-situ* Fe isotope ratio determination in Fe-Ti oxides and sulfides from drilled gabbros and basalt from the IODP Hole 1256D in the eastern equatorial Pacific. *Chem Geol*, 363: 101–113
- Gao G L, Zhang W, Zhou L B, Wang L J. 2013. The research on transformation rule of heavy metal migration in lead-zinc tailings reservoir of QiaoKuo. *Nonfer Metals Eng*, 3: 41–44
- Götte T, Richter D. 2006. Cathodoluminescence characterization of quartz particles in mature arenites. *Sedimentology*, 53: 1347–1359
- Götze J. 2012. Application of cathodoluminescence microscopy and spectroscopy in geosciences. *Microsc Microanal*, 18: 1270–1284
- Gucsik A, Koeberl C, Brandstatter F, Reimold W U, Libowitzky E. 2002. Cathodoluminescence, electron microscopy, and Raman spectroscopy of experimentally shock-metamorphosed zircon. *Earth Planet Sci Lett*, 202: 495–509
- Habermann D, Neuser R D, Richter D K. 1996. REE-activated cathodoluminescence of calcite and dolomite: High resolution spectrometric analysis of CL emission (HRS-CL). *Sediment Geol*, 101: 1–7
- Hanchar J M, Rudnick R L. 1995. Revealing hidden structures: The application of cathodoluminescence and back-scattered electron imaging to dating zircons from lower crustal xenoliths. *Lithos*, 36: 289–303
- Humphreys J. 2004. Reconstruction of grains and subgrains from electron backscatter diffraction maps. *J Microsc*, 213: 247–256
- Jin Z M, Zhang J, Green H W, Jin S. 2001. Eclogite rheology: Implications for subducted lithosphere. *Geology*, 29: 667–670
- Jung H, Karato S. 2001. Water-induced fabric transitions in olivine. *Science*, 293: 1460–1463
- Katayama I, Jung H, Karato S. 2004. New type of olivine fabric from deformation at modest water content and low stress. *Geology*, 32: 1045–1048
- Kayama M, Nakano S, Nishido H. 2010. Characteristics of emission centers in alkali feldspar: A new approach by using cathodoluminescence spectral deconvolution. *Am Mineral*, 95: 1783–1795
- Li G C, Xiao K. 2012. Distribution characteristics of minerals and elements in chromite ore processing residue. *Trans Tianjin Univ*, 2012, 18: 052–056
- Lissenberg C J, Rioux M, Shimizu N. 2009. Zircon dating of oceanic crustal accretion. *Science*, 323: 1048–1050
- Mancktelow N, Grujic D, Johnson E. 1998. An SEM study of porosity and grain boundary microstructure in quartz mylonites, Simplon Fault Zone, Central Alps. *Contrib Mineral Petrol*, 131: 71–85
- Mitchell R H, Xiong J, Mariano A N, Fleet M E. 1997. Rare-earth-element-activated cathodoluminescence of apatite. *Can Mineral*, 35: 979–998
- Nasdala L, Zhang M, Kempe U, Panczer G, Gaft M, Andrut M, Plotze M. 2003. Spectroscopic methods applied to zircon. *Rev Mineral Geochem*, 53: 427–267
- Prior D J, Boyle A, Brenker F, Cheadle M C, Day A, Lopez G, Peruzzo L,

- Potts G J, Reddy S, Spiess R. 1999. The application of electron backscatter diffraction and orientation contrast imaging in the SEM to textural problems in rocks. *Am Mineral*, 84: 1741–1759
- Rajkumar K, Ramanathan A L, Behera P N, et al. 2014. Preliminary studies on the characterization of clay minerals in the Sundarban mangrove core sediments, West Bengal, India. *Arab J Geosci*, 7: 537–544
- Richter D K, Götze T, Habermann D. 2002. Cathodoluminescence of authigenic albite. *Sediment Geol*, 150: 367–374
- Smieja-Król B, Fialkiewicz-Kozielec B. 2014. Quantitative determination of minerals and anthropogenic particles in some Polish peat occurrences using a novel SEM point-counting method. *Environ Monit Assess*, 186: 2573–2587
- Stöckhert B, Duyster J, Trepmann C. 2001. Microdiamond daughter crystals precipitated from supercritical CO₂ silicate fluids included in garnet, Erzgebirge, Germany. *Geology*, 29: 391–394
- Su L, Song S G, Song B, Zhou D W, Hao J R. 2004. SHRIMP zircon U-Pb ages of garnet pyroxenite and Fushui gabbroic complex in Songshugou region and constraints on tectonic evolution of Qinling Orogenic Belt. *Chin Sci Bull*, 49: 1307–1310
- Vavra G, Gebauer D, Schmid R, Compston W. 1996. Multiple zircon growth and recrystallization during polyphase Late Carboniferous to Triassic metamorphism in granulites of the Ivrea Zone (Southern Alps): An ion microprobe (SHRIMP) study. *Contrib Mineral Petrol*, 122: 337–358
- Vavra G, Schmid R, Gebauer D. 1999. Internal morphology, habit and U-Th-Pb microanalysis of amphibolite-to-granulite facies zircons: Geochronology of the Ivrea Zone (Southern Alps). *Contrib Mineral Petrol*, 134: 380–404
- Wang L J. 2005. Tubal character and modification of natural chrysotile. Doctoral Dissertation. Beijing: Peking University. 25
- Wilde S A, Valley J W, Peck W H, Graham C M. 2001. Evidence from detrital zircons for the existence of continental crust and oceans on the earth 4.4 Gyr ago. *Nature*, 409: 175–178
- Wu Y Q, Cui Z J, Liu G N, Ge D K. 1996. Sepimental feature of loss and climate change in the col area of Kunlunshan Mountain. *J Guizhou Normal Univ (Nature Science)*, 14: 20–24
- Xiao X C, Wang J, Su L, Song S G. 2003. A further discussion of the Kuda ophiolite, West Kunlun, and its tectonic significance. *Geol Bull China*, 22: 745–750
- Xie Y Y, Cui Z J. 1981. Some surfacial characteristics of till quartz sand in China under electronic scanning microscope. *J Glaci Geocry*, 3: 52–55
- Xu Z Q, Chen J, Yang J S, Li X P, Chen F Y. 2003. Discovery of titanoclinohumite and titanochondrodite exsolution in clinopyroxene included in garnet peridotite and their significance. *Acta Geol Sin*, 77: 549–555
- Xu Z Q, Chen J, Wang Q, Zeng L S, Yang J S, Chen F Y, Li T F, Liang F H. 2005. Type-C olivine fabric in the Zhimafang garnet peridotite of the southern Sulu ultrahigh-pressure metamorphic terrane: Formation conditions and tectonic implications. *Acta Petrol Sin*, 21: 389–397
- Xu Z Q, Wang Q, Liang F H, Chen F Y, Xu C P. 2009. Electron backscatter diffraction (EBSD) technique and its application to study of continental dynamics. *Acta Petrol Sin*, 25: 1721–1736
- Yang T N, Zeng L S, Liou J G. 2005. Mineral evolution of a garnet-pyroxene nodule within eclogite, eastern Sulu ultrahigh-pressure metamorphic terrane, East China. *J Metamorph Geol*, 23: 677–680
- Ye K, Cong B L, Ye D N. 2000. The possible subduction of continental material to depths greater than 200 km. *Nature*, 407: 734–736
- Zhang G B, Zhang L F, Christy A, Song S G, Li Q L. 2014. Differential exhumation and cooling history of North Qaidam UHP metamorphic rocks, NW China: Constraints from zircon and rutile thermometry and U-Pb geochronology. *Lithos*, 205: 15–27
- Zhang G B, Ellis D J, Christy A G, Zhang L F, Niu Y L, Song S G. 2009. UHP metamorphic evolution of coesite-bearing eclogite from the Yuka terrane, North Qaidam UHPM belt, NW China. *Eur J Miner*, 21: 1287–1300
- Zhang G B, Niu Y L, Song S G, Zhang L F, Tian Z L, Christy A, Han L. 2015. Trace element behavior and *P-T-t* evolution for partial melting of exhumed eclogite in the North Qaidam UHPM belt (NW China): Implications for adakite genesis. *Lithos*, 226: 65–80
- Zhang J F, Jin Z M, Green H W. 2005. Hydroxyl induced eclogite fabric and deformation mechanism. *Chin Sci Bull*, 50: 685–690
- Zhang S Q, Karato S, Fitz J, Faul U, Zhou Y. 2000. Simple shear deformation of olivine aggregates. *Tectonophysics*, 316: 133–152
- Zhang X H, Su L, Cui X J. 2008. Metallogenetic epoch and mechanism of the tungsten ore in Yushan, Beishan orogenic belt, Gansu. *Chin Sci Bull*, 53: 1222–1230
- Zhou D W, Su L, Jian P, Wang R S, Liu X M, Lu G X, Wang J L. 2004. Zircon U-Pb SHRIMP ages of high-pressure granulite in Yushugou ophiolitic terrane in southern Tianshan and their tectonic implications. *Chin Sci Bull*, 49: 1415–1419
- Zhu Y F, Ogasawara Y. 2002. Carbon recycled into the deep Earth: Evidenced by dolomite dissociation in subduction-zone rocks. *Geology*, 30: 947–950